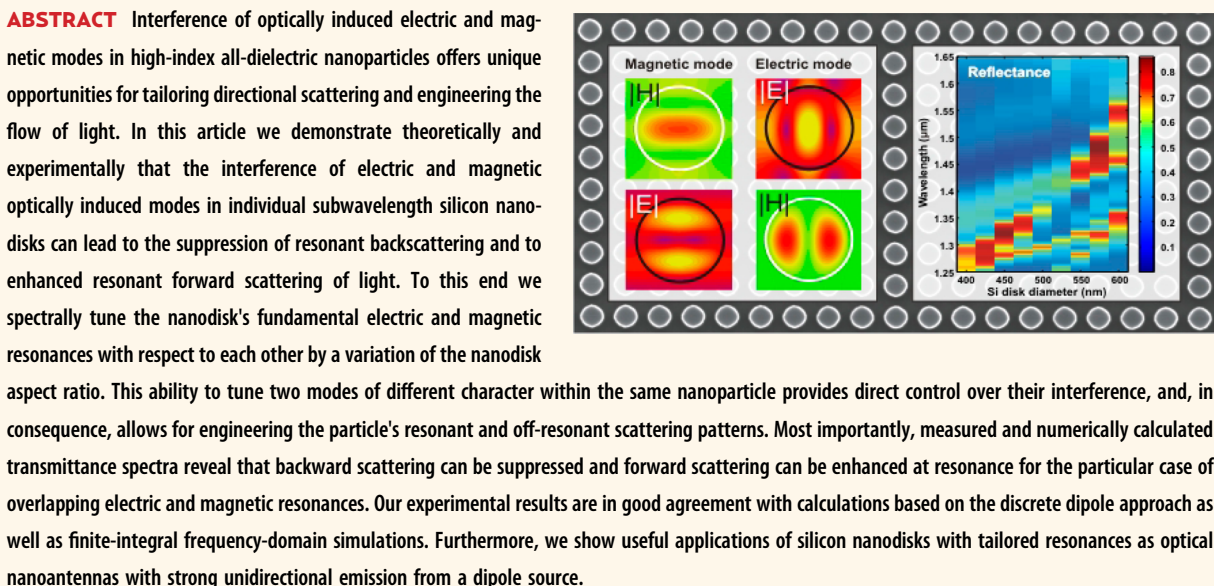


Tailoring Directional Scattering through Magnetic and Electric Resonances in Subwavelength Silicon Nanodisks

Isabelle Staude,^{†,‡,*} Andrey E. Miroshnichenko,[†] Manuel Decker,[†] Nche T. Fofang,[‡] Sheng Liu,[‡] Edward Gonzales,[‡] Jason Dominguez,[‡] Ting Shan Luk,[‡] Dragomir N. Neshev,[†] Igal Brener,[‡] and Yuri Kivshar[†]

[†]Nonlinear Physics Centre, Research School of Physics and Engineering, The Australian National University, Canberra ACT 0200, Australia and [‡]Center for Integrated Nanotechnologies, Sandia National Laboratory, Albuquerque, New Mexico 87185, United States



KEYWORDS: magnetic resonance · all-dielectric nanoantennas · nanodisks · directional scattering · resonant scattering

The ability to manipulate light at the nanoscale is the cornerstone for a wide range of applications including compact photonic devices and their dense integration on an optical chip. However, at subwavelength dimensions conventional optical elements lose their functionality, creating the need for entirely new concepts to control and utilize light at the nanoscale. While plasmonic nanostructures are widely recognized for their ability to concentrate light to deep-subwavelength volumes,^{1–3} they suffer from intrinsic nonradiative optical losses in metals at optical frequencies, limiting their efficiency for key applications like quantum-light sources, photovoltaics, sensing, and metamaterials. These losses become particularly relevant for more

complex plasmonic device geometries which comprise larger amounts of metal, like for example, arrayed nanoantennas for unidirectional emission enhancement.^{4–8}

Thus, an alternative implementation of subwavelength optics other than nanoplasmonics is highly desired for the development of efficient nanophotonic devices. Recent experimental demonstrations of strong resonant response from subwavelength high-index all-dielectric particles in the visible and infrared spectral range^{9–16} suggest such a novel approach to nanophotonics. The observed optically induced resonances can be employed in a similar way as plasmonic resonances of metallic nanoparticles and may allow overcoming the problem of strong losses in plasmonic

* Address correspondence to ips124@physics.anu.edu.au.

Received for review May 30, 2013 and accepted August 16, 2013.

Published online August 16, 2013
10.1021/nn402736f

© 2013 American Chemical Society

structures paving a way toward low-loss nanophotonic devices based on all-dielectric or hybrid metal–dielectric metamaterials^{17–19} and nanoantennas.^{20–23}

Importantly, high-index dielectric nanoparticles support both electric and strong magnetic resonances.^{9–16} This is in contrast to highly symmetric metallic nanoparticles, where resonant scattering is dominated by electric resonances only.²⁴ To obtain a magnetic optical response from plasmonic nanoparticles, more complex particle geometries like split-ring resonators²⁵ that support a circular current are necessary.

Despite the different geometries of all-dielectric nanoparticles supporting magnetic resonances compared to their plasmonic counterparts the basic physics of the magnetic response of high-index dielectric nanoparticles is quite similar to that of conventional metallic split-ring resonators: in a dielectric nanoparticle, a magnetic Mie resonance originates from the excitation of a particular electromagnetic mode inside the particle, which exhibits a circular displacement current of the electric field.¹⁷ This mode is excited when the effective wavelength of light inside the particle becomes comparable to the particle's size. It is characterized by an antiparallel orientation of the electric field at opposite sides of the particle and a maximum of the magnetic field at its center. The study of such magnetic Mie resonances in all-dielectric nanoparticles¹⁰ and tailoring at will their interplay with the nanoparticle's electric Mie resonances open many new possibilities for light manipulation at the nanoscale. For example, dielectric nanoparticles with strong magnetic response support a new type of resonant interaction at the nanoscale including a novel manifestation of Fano resonances,²⁶ which were previously extensively studied in plasmonic systems.^{27–30}

The capability of having both electric and magnetic modes within a single nanoparticle is of particular interest. Not only is a simultaneous electric and magnetic optical response the key ingredient for most photonic metamaterials.^{17–19} Even more importantly, interference between electric and magnetic modes can lead to strong effects on the particle's scattering properties³¹ including surprising *directional radiation effects*.^{32–34} Hence, tailoring optically induced modes of all-dielectric nanoparticles and their interference offers intriguing applications for nanophotonic devices like nanoantennas, sensing, and photovoltaics. For example, unidirectional scattering was recently experimentally demonstrated through the off-resonant overlap of electric and magnetic optical modes^{15,35,36} where the observed behavior was found to be similar to Kerker-type light scattering³⁷ by hypothetical magneto-dielectric particles. However, if the operating spectral regime is far from the resonance, scattering is generally weak in all directions, and no significant forward scattering enhancement can be observed.³⁸

Resonant scattering, in contrast, brings the advantages of a large scattering cross section of the particle over a broad spectral range (comparable to the resonance width) for plane-wave excitation.³⁸ Usual resonant scattering, however, is symmetric in the forward and backward directions. Hence, to suppress backward scattering, geometries that employ various types of auxiliary elements or rely on interaction with a substrate have been demonstrated.^{4–8,39,40} We show that the introduction of such additional elements is not necessary for nanoparticles that support spectrally overlapping electric and magnetic resonances. Remarkably, backward scattering can even be completely canceled if the two overlapping resonances have the same strength.³⁸ While this concept has been theoretically analyzed for carefully designed metal–dielectric core–shell nanoparticles,³⁸ an all-dielectric, metal-free implementation of such resonant forward scattering has neither been suggested nor demonstrated so far.

Instead, most of the current studies of the magnetic response of dielectric nanoparticles, including experimental demonstrations,^{12–15} concentrate on designs based on high-permittivity dielectric spheres^{12,13,15} or cubes.¹⁴ Such three-dimensional shapes are governed by only one geometrical parameter, and thus do not allow for spectrally shifting the resonance positions of the electric and magnetic lowest-order Mie-type modes with respect to each other. Instead, the fundamental mode of a high-index dielectric sphere or cube is always of the magnetic dipole type,¹³ and it occurs at a different frequency from the electric one. The same holds true for dielectric pillars, where the lateral diameter and the height are comparable.³⁵ Consequently, for such particles with spectrally separate resonances directional scattering can only be observed in the off-resonant regime. It is therefore an open challenge to tailor the respective spectral position of the electric and magnetic modes in high-index dielectric nanoparticles in order to utilize at will either their electric, magnetic, or combined magneto-electric polarizabilities at resonance.

To achieve this goal, we here consider disk-shaped silicon nanoparticles which offer the opportunity both to select either the electric or the magnetic single-particle Mie-type mode as the lowest-order resonance and to tune their relative spectral positions by simply adjusting the disk height-to-diameter aspect ratio.⁴¹ Most importantly, choosing the appropriate aspect ratio also allows for bringing the two lowest-order (electric and magnetic dipole) resonances into spectral overlap. Using silicon nanodisks embedded into a low-index homogeneous medium, we demonstrate this resonance overlap of electric and magnetic modes experimentally for the first time to our knowledge. Furthermore, we observe the effect of this overlap on far-field transmittance and reflectance spectra, where it leads to suppressed backward scattering

and therefore to high optical transmission through the structure despite two pronounced resonances being excited at the overlap spectral position at the same time. This has important implications for unidirectional nano-antennas, which utilize the interference of scattering from different modes within the same nanoparticle.⁴² Using numerical simulations we study the capability of a single nanodisk to act as an interference-based nano-antenna, revealing that the ability to tailor the relative spectral mode positions can indeed enable a fundamentally new, highly directional type of such devices.

RESULTS AND DISCUSSION

Discrete Dipole Description of the System. To demonstrate the individual control of the electric and magnetic dipole resonances in silicon nanodisks, first we calculate the extinction spectra of the electric and magnetic modes supported by a single silicon nanodisk using the theoretical method developed by Evlyukhin *et al.*⁴¹ This approach is based on the discrete-dipole approximation (DDA), and it allows for decomposition at the extinction cross-section of an arbitrary shaped nanoparticle into its constituent multipole contributions, including the lowest order magnetic and electric dipole modes.⁴¹ Our approach enables us to rigorously analyze the role of multipole modes in the extinction spectra of silicon nanodisks for any value of the disk aspect ratio.

To this end, we represent the scattering object, for example, our silicon nanodisk, by a cubic lattice of optically small elements with corresponding electric point dipoles with local polarizability α_p .⁴³ For a monochromatic field the electric dipole moments \mathbf{P}_j induced in each lattice point j are then determined by the self-consistent coupled-dipole equations⁴¹

$$\mathbf{P}_j = \alpha_p \mathbf{E}_0(\mathbf{r}_j) + \alpha_p \frac{k_0^2}{\varepsilon_0} \sum_{l \neq j}^N \hat{G}(\mathbf{r}_j, \mathbf{r}_l) \mathbf{p}_l \quad (1)$$

where $\mathbf{E}_0(\mathbf{r}_j)$ is the external electric field at position \mathbf{r}_j , k_0 is the vacuum wavenumber, ε_0 is the vacuum permittivity, \hat{G} is the Green's tensor of the medium surrounding the scatterer, and N is the total number of point dipoles in the system. The total extinction cross section σ_{ext} of the lowest order electric and magnetic dipole modes can then be expressed by⁴¹

$$\begin{aligned} \sigma_{\text{ext}} &\approx \sigma_{\text{ext}}^{\text{p}} + \sigma_{\text{ext}}^{\text{m}} \\ \sigma_{\text{ext}}^{\text{p}} &= \frac{k_b}{\varepsilon_0 \varepsilon_b |\mathbf{E}_0|^2} \text{Im}(\mathbf{E}_0^*(\mathbf{r}_0) \cdot \mathbf{p}), \\ \sigma_{\text{ext}}^{\text{m}} &= \frac{k_b}{\varepsilon_b |\mathbf{H}_0|^2} \text{Im}(\mathbf{H}_0^*(\mathbf{r}_0) \cdot \mathbf{m}) \end{aligned} \quad (2)$$

where ε_p is the permittivity and k_p is the wavenumber of the background medium, and

$$\mathbf{p} = \sum_{j=1}^N \mathbf{p}_j, \quad \mathbf{m} = \sum_{j=1}^N \mathbf{m}_j(\mathbf{r}_0) \quad (3)$$

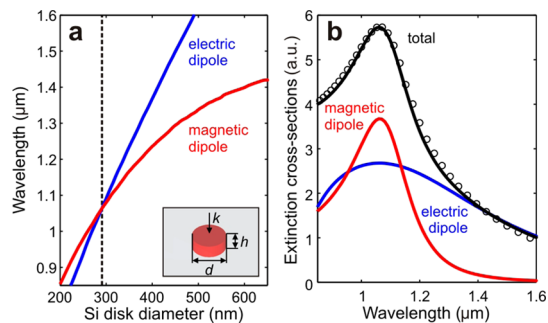


Figure 1. (a) Traced spectral maxima positions of extinction cross sections derived from calculations based on discrete dipole approximation (DDA) for the electric (blue line) and magnetic (red line) dipole moments of a single silicon nanodisk with height $h = 220$ nm embedded into a low-index medium ($n_b = 1.5$). The extinction cross section maxima associated with the electric and magnetic resonance can be brought into spectral overlap for $d \approx 290$ nm as indicated by the black dashed line. The inset shows a sketch of the considered geometry. (b) Calculated extinction cross sections for the case of resonance overlap. Solid lines depict results of DDA calculations, the circles show results obtained by finite-integral frequency-domain (FIFD) calculations for comparison.

Here $\mathbf{m}_j(\mathbf{r}_0) = \omega/(2i)(\mathbf{r}_j - \mathbf{r}_0) \times \mathbf{p}_j$ is the magnetic dipole moment located at \mathbf{r}_0 associated with the electric dipole \mathbf{p}_j .

Figure 1a shows the maxima positions of the extinction cross sections calculated using eq 2 for the electric and magnetic dipole modes, respectively, of silicon disks with $h = 220$ nm height and diameters ranging from $d = 200$ nm to $d = 650$ nm. According to the Mie theory for spherical particles, the magnetic dipole resonance takes place when the effective wavelength of light inside the particle equals its diameter.¹³ For the case of cylindrical particles the spectral electric and magnetic mode positions are dependent on both the height and the diameter, and they can be analytically estimated utilizing magnetic wall boundary conditions.⁴⁴ From this it is expected that the electric resonance position exhibits a much stronger wavelength shift with respect to the nanodisk diameter as compared to the shift of the magnetic dipole resonance. This difference in the magnitude of the spectral shifts, which we indeed observe in our results, leads to the ability to overlap the two extinction maxima. In our case, the overlap condition is fulfilled for $d \approx 290$ nm, corresponding to an aspect ratio of $\chi = h/d = 0.76$, for a single silicon nanodisk. The electric, magnetic, and total extinction spectra for this case calculated by DDA (solid lines) are plotted in Figure 1b, clearly showing the spectral overlap of both modes at a vacuum wavelength of $\lambda \approx 1060$ nm. Figure 1b furthermore includes the result of a numerical finite-integral frequency-domain (FIFD) calculation (CST microwave studio, open boundary conditions) of the total extinction cross-section of an identical single silicon nanodisk for comparison (circles). We have confirmed that the same excellent agreement found in Figure 1b for the two different numerical methods is

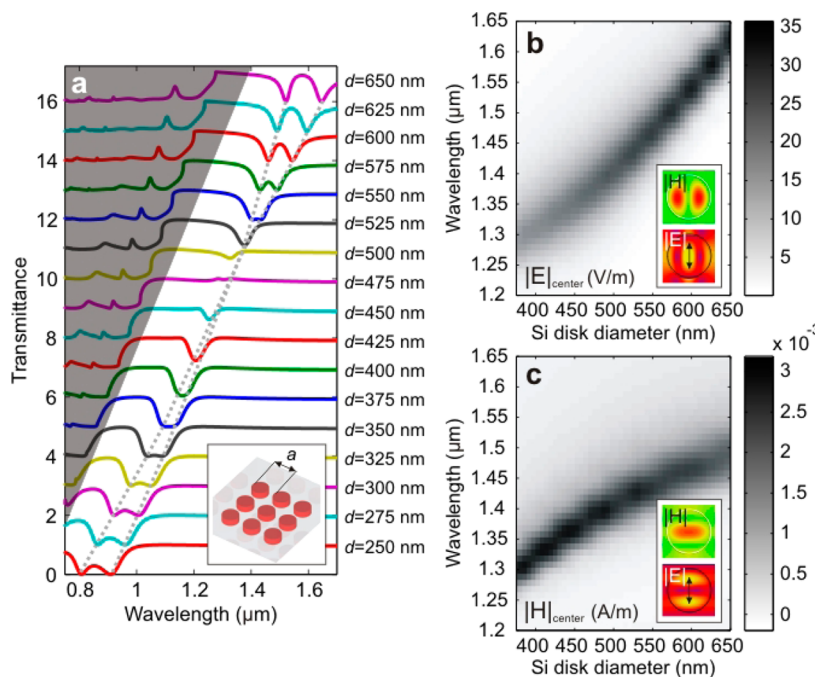


Figure 2. (a) Numerically calculated linear-optical transmittance spectra for arrays of embedded silicon disks (see inset) with height $h = 220$ nm and variable lattice constant ($a = d + 200$ nm), revealing a complete mode crossing with spectrally separate resonances on both sides of the overlap. For clarity spectra are vertically displaced by $T = 1$ each time the disk diameter is increased by 25 nm. The dashed lines are guides to the eye. Spectral features arising from the diffraction by the lattice are grayed out. (b) Calculated electric and (c) magnetic field magnitude at the silicon disk center for $a = 800$ nm. The insets show the electric and magnetic mode profiles for $d = 650$ nm.

obtained over the entire range of disk diameters from 200 to 650 nm.

Numerical Calculation. Next we consider an array of silicon nanodisks, which allows for easier experimental characterization of the modes in comparison to single particle extinction measurements.⁴⁵ To investigate the manifestation of the mode properties in the optical spectra of silicon disk arrays and to gain an additional insight into the properties of the observed modes, we perform FIFD calculations using CST Microwave Studio. We use periodic boundary conditions where the lattice constant a is varied together with the diameter d , setting $a = d + 200$ nm. The height of the silicon disks remains unchanged ($h = 220$ nm). The refractive index of the silicon disks is $n = 3.5$, and of the substrate and the embedding medium $n_b = 1.5$. Air interfaces are neglected. For calculating transmittance $T(\lambda)$ we use normal-incidence plane-wave excitation and evaluate the power flow through the sample. For the lossless system, this allows us to obtain the total reflectance R as $1 - T$. The calculated transmittance spectra are plotted in Figure 2a, showing the crossing of the two modes with the change of the disk diameter. Note the near-perfect suppression of backward scattering observed for the case of mode overlap at $d \approx 475$ nm, where the transmittance approaches a flat $T = 1$ line. We also calculate the electric and magnetic mode profiles at resonant conditions in a cut plane through the center of the disk for $d = 650$ nm and $a = 800$ nm where the two dips are well separated. These results

are shown in the insets of Figure 2 panels b and c. The lowest order (i.e., lowest frequency) resonance for low-aspect ratio (i.e., larger diameter) disks [see Figure 2b] clearly exhibits electric characteristics with the magnetic field showing a node and the electric field showing an antinode at the center. The next higher order mode for low-aspect ratio disks, in contrast, exhibits the opposite behavior, with the magnetic field showing an antinode and the electric field showing a node at the disk center [see inset in Figure 2c]. Making use of these distinct characteristics of the mode profiles, we plot the absolute value of electric and magnetic fields at the center of the silicon nanodisks for different disk diameters in Figure 2 panels b and c, respectively. Here, the lattice constant is fixed to $a = 800$ nm for direct comparison with experimental data. Again, in support of our results obtained by DDA, the electric and magnetic resonances and their crossing can clearly be identified. Differences in the spectral overlap positions derived from the DDA calculations for extinction cross sections of single silicon nanodisks and from the FIFD simulations for near-field enhancement at the disk center for silicon nanodisk arrays are partly due to lattice interactions and partly due to the different methods used to estimate the resonant wavelength. In the first case the resonant wavelengths of the electric and magnetic modes are estimated by the lowest-order maxima positions of the respective extinction cross section contributions. It is known that the spectral positions of extinction maxima can be significantly

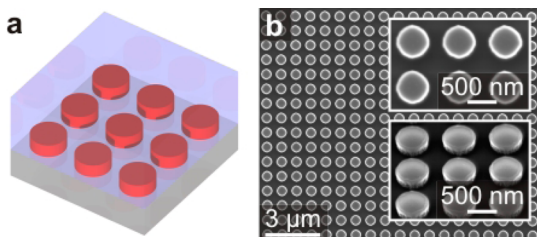


Figure 3. (a) Sketch of the silicon nanodisks embedded into a low-index matrix. (b) Scanning electron micrograph of typical fabricated silicon nanodisks before embedding them into the low-index medium. The insets show magnified (top) and oblique-incidence (bottom) views.

shifted with respect to the actual eigenfrequencies of the resonant mode due to various interference phenomena such as Fano resonance etc.⁴⁶ In the second case we estimate the resonant wavelengths of the electric and magnetic modes *via* the resonant behavior of the electric and magnetic field enhancements at the nanodisk center. This method is only an approximate method as well as it does not capture the exact mode profile.

Experimental Results. We fabricated silicon nanodisk arrays on silicon oxide using electron-beam lithography on silicon-on-insulator wafers in combination with directive reactive-ion etching. In a subsequent step we embedded the silicon nanodisks in a low-refractive-index medium. Details of the fabrication procedure can be found in the Methods section. As the height of the disks is fixed to the top silicon layer thickness of our SOI wafer ($h = 220$ nm), we vary the aspect ratio by changing only the diameter of the silicon disks while keeping their height constant. The diameter d of the disks is systematically varied between 400 nm and 600 nm, resulting in disk aspect ratios $\chi = h/d$ ranging from 0.55 to 0.37. The lattice constant of the array is $a = 800$ nm. This choice of densely packed disks not only ensures a strong far-field signature in transmittance measurements, but also allows for studying the particle resonances with only a small influence from grating effects, as the lowest order diffractive mode occurs at shorter wavelengths as compared to the resonance frequencies of interest. While the close proximity of neighboring disks has an influence on the exact resonance positions of the silicon disk, the resonances follow the same qualitative behavior observed for a single particle, as seen in Figure 1. A schematic of the studied geometry and scanning electron micrographs of a typical fabricated silicon disk array before the disks are imbedded are displayed in Figure 3a,b, respectively, for $d \approx 550$ nm.

We measure linear-optical transmittance and reflectance spectra both for the embedded and for the free-standing silicon disk arrays using a custom-built white-light spectroscopy setup connected to an optical spectrum analyzer. Transmittance [Reflectance] is understood as $T = I_T(\lambda)/I_{T,0}(\lambda)$ [$R = I_R(\lambda)/I_{R,0}(\lambda)$], where $I_T(\lambda)$ [$I_R(\lambda)$] is the transmitted [reflected]

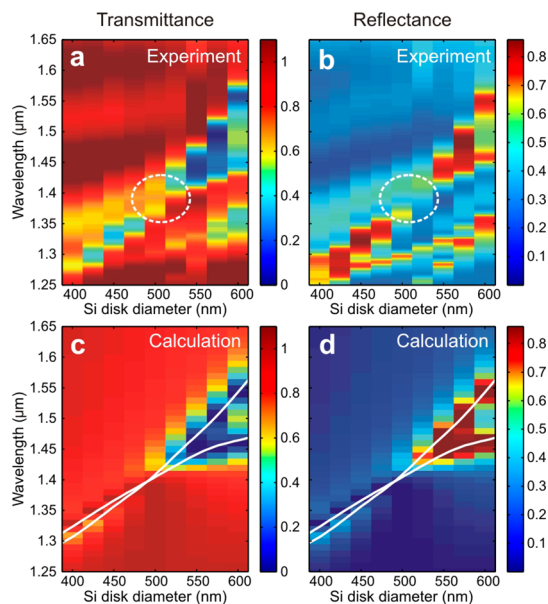


Figure 4. Experimentally measured optical transmittance (a) and reflectance (b) spectra for silicon nanodisks with height $h = 220$ nm embedded into a low-index medium. The disk aspect ratio is systematically varied in order to tune the electric and magnetic resonances into spectral overlap. The white dashed ellipses indicate the regions where the depth/height of the overlapping resonance minima/maxima is significantly reduced compared to the isolated resonances. This is attributed to the suppression of resonant backward scattering through destructive interference of simultaneously excited electric and magnetic modes in each individual silicon nanodisk. (c,d) Corresponding numerically calculated transmittance and reflectance spectra, respectively. The white solid lines show the resonance positions for separately calculated electric and magnetic response shown in Figure 2b,c.

wavelength-dependent intensity arriving at the detector when the sample is inserted into the beam path, and $I_{T,0}(\lambda)$ [$I_{R,0}(\lambda)$] is the transmitted [reflected] wavelength-dependent intensity arriving at the detector when the reference is inserted into the beam path. A pair of 20 \times Mitutoyo Plan Apo NIR infinity-corrected objectives with numerical aperture NA = 0.4 is used to focus the incident light onto the sample and to collect the light transmitted through the sample. As no higher diffraction orders exist in the spectral range of interest for the relevant lattice constant most of the transmitted light is collected by the second objective. The range of incident angles has been reduced to ± 6 degrees by an aperture. In reflectance, the light is collected by the same objective used for focusing. The transmittance and reflectance measurements are referenced to the transmittance of the unstructured wafer next to the silicon disk arrays and to the reflectance of a silver mirror, respectively. Transmittance values exceeding unity are due to the referencing procedure in the presence of Fabry–Perot resonances in the spectra of the layered wafer structure. The measured spectra for the embedded disks are shown in Figure 4a,b. Two distinct resonances can clearly be identified for the largest fabricated disk diameter of

$d \approx 600$ nm both in transmittance and in reflectance. On the basis of the Beer–Lambert law such resonant suppression of the transmission through a 2D periodic array can be linked to the extinction cross-section of a single nanodisk by $T \approx \exp(-\sigma_{\text{ext}}/a^2)$. Here, T is the fraction of the intensity that goes through the structure without being scattered or absorbed, while the transmittance measured in our experiment and calculated in numerical simulations allows for a finite range of collection angles. However, for a two-dimensional periodic array of silicon disks with a lattice constant sufficiently small as to not generate higher propagating diffraction orders in the spectral range of interest, both definitions of transmittance give equivalent results. The physical reason for this is that the non-normal components of scattered light cancel out in the far-field for a periodic array of azimuthally symmetric scatterers driven in phase. At resonance, for spectrally well separated resonances, we observe $T \approx 0$, which can be interpreted as destructive interference in the forward direction of incident and resonantly induced scattered waves which originate from the electric and magnetic particle resonances. The two resonances move closer together as the disk diameter decreases and merge at around $d \approx 500$ nm. Remarkably, at the point of overlap, instead of getting more pronounced, the transmission dip and the reflectance peak become significantly smaller, making the whole structure more transparent (see regions within white dashed ellipses in Figure 4a,b). The reason for this surprising behavior is that for overlapping electric and magnetic resonances destructive interference of incident and scattered waves now takes place in the backward direction. In other words, the structure comes closer to satisfying the impedance matching condition for free space ($\epsilon = \mu$) when exhibiting both an electric and a magnetic response within the same frequency range. This leads to less light being reflected, and, consequently, more light being transmitted through the structure. Such impedance matching effect observed for our arrays is equivalent to the suppression of backscattering for single particles. Note here, that in this situation Beer–Lambert law does not work since transmission $T \approx 1$ implies zero extinction cross-section of a single nanodisk $\sigma_{\text{ext}} = 0$, which is not the case (see Figure 1). The reason for this is that at the resonance overlap the amplitude of the total scattered wave (electric and magnetic resonance) is twice the amplitude of the incident one, and they interfere destructively with each other. This implies that despite the fact that $T \approx 1$ the amplitude of the transmitted wave is out of phase with the incident wave, indicating that we are still dealing with a resonant effect.

To directly compare our experimental measurements with theory, we numerically calculate transmittance and reflectance spectra for the given experimental parameters. The calculated spectra are displayed in

Figure 4c,d, showing a good general agreement with the experimental measurements. The main differences between experimental and numerical data arise from Fabry–Perot resonances in the layered wafer structure, which lead to several additional local extrema in the measured spectra, for example, transmittance minima/reflectance maxima around 1.35 and 1.55 μm wavelength. The layered wafer structure was not modeled in the numerical calculations in order to keep the size of the computational domain sufficiently small to allow for realistic computation times. Furthermore, an additional signature of low transmittance and high reflectance is present in the experimental curves at the short wavelength side of the resonances, which can be attributed to coupling to higher-order modes. This becomes possible for not strictly normal incidence in the experiment. Any additional differences between experimental and numerical spectra are likely due to a combination of fabrication inaccuracies and the finite range of incident angles used in experiment. Fabrication inaccuracies include deviations from a perfect circle shape of the silicon nanodisks in top view as well as surface roughness and not entirely straight sidewalls. The white solid lines mark the smoothed maximum positions from Figure 2b,c, showing the overlap/crossing at $d \approx 500$ nm. It is worth noting that the spectral resonance positions, including that of the resonance overlap, are shifted upon changing the lattice constant a or when comparing single disks with disks arranged in an array. Furthermore, because the resonances blue shift and approach the first Wood's anomaly as the disk diameter is reduced, the mode separation on the small-diameter side of the mode crossing is smaller in our system with $a = 800$ nm as compared to the results presented in Figure 2a. However, this is not representative for the behavior of the silicon nanodisks as such. As obvious from Figure 1a,b for single disks and from Figure 2a for arrays with varying lattice constant, a clear separation of the two modes can be observed on both sides of the overlap. Here, as the electric and magnetic mode start moving out of spectral overlap again for small disk diameters, although they are still too close to produce two spectrally separate transmittance minima and reflectance maxima, a clear signature shows up again in the transmittance/reflectance spectra as backward scattering is not suppressed anymore.

For comparison we have also measured and calculated transmittance and reflectance spectra for a nominally identical sample with arrays of free-standing (not embedded) nanodisks. These results are shown in Figure 5 panels a and b, respectively. The calculated spectra are displayed in Figure 5c,d, showing very good agreement with the experimental measurements. The free-standing disks exhibit the same effect of reduced backward scattering for overlap of the electric and magnetic resonance around $d \approx 525$ nm as observed for the embedded disks. While a theoretical description

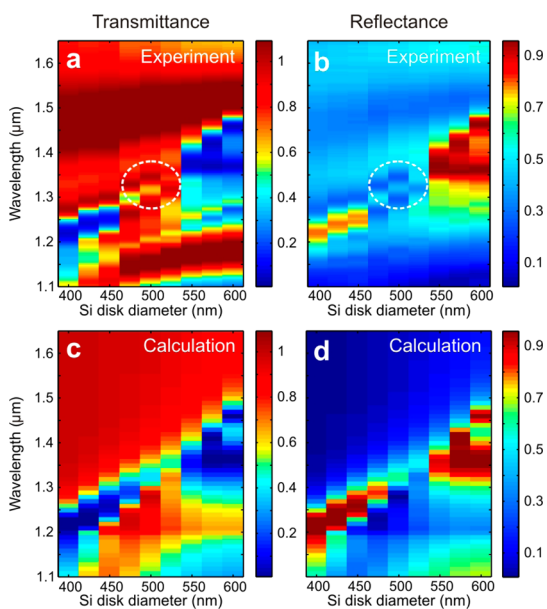


Figure 5. Experimentally measured optical transmittance (a) and reflectance (b) spectra for free-standing (not embedded) silicon nanodisks with height $h = 220$ nm on silicon oxide. The spectral overlap of the electric and magnetic resonances occurs for $d \approx 525$ nm, resulting in reduced backward scattering (see areas marked by white ellipses). (c) Corresponding numerically calculated transmittance and (d) reflectance spectra.

of silicon disks on a substrate is challenging compared to that of disks embedded into a homogeneous medium, these results show that the suppression of backward scattering through interference of the electric and magnetic modes in the silicon nanodisks with the incident light wave is robust against changes in the dielectric environment of the disks.

The observed resonant forward scattering effect could be useful for solar cells, antireflection coatings, and high-transmission phase modulators. Importantly, however, potential applications of optical mode interference in silicon nanodisks are not limited to the case of mode overlap. In the next section we demonstrate through numerical simulations that the capability to shift the modes with respect to each other also proves useful for optimizing scattering properties in the off-resonant regime, and that our findings have important implications for a new type of all-dielectric directional nanoantennas.

Implications for Single-Element All-Dielectric Nanoantennas

Even a single embedded disk can already act as a broadband unidirectional nanoantenna exhibiting an ultrahigh front-to-back-ratio (FBR) based on an off-resonant interference phenomenon between tailored electric and magnetic modes excited by an electric dipole point source. Such a geometry is illustrated in Figure 6a. In the dipole approximation, we can analytically derive the expression for FBR in the limit of closely placed dipole-like emitters. The FBR is equal to $|\langle \alpha_E - ib\kappa\alpha_H \rangle / (\alpha_E + ib\kappa\alpha_H)|^2$, where α_E and α_H are the

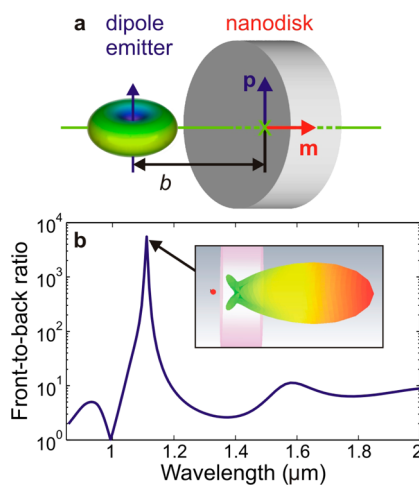


Figure 6. (a) Sketch of a single embedded silicon nanodisk used as a highly directive optical nanoantenna (not to scale). (b) Numerically calculated front-to-back ratio (FBR) for an electric dipole emitter coupled to a single embedded silicon nanodisk supporting tailored electric and magnetic resonances. The emitter is axially displaced from the disk center by $b = 155$ nm. The inset shows the emission pattern at maximum FBR.

effective electric and magnetic polarizabilities of the single nanodisk, k is the vacuum wavenumber, and b is the separation between the electric dipole emitter and the nanodisk center. This expression indicates that at the corresponding resonance the FBR can be greatly enhanced due to vanishing denominator.

Figure 6b shows the FBR for an electric dipole emitter coupled to a silicon nanodisk of diameter $d = 620$ nm calculated numerically using CST Microwave Studio. The emitter is axially displaced from the center of the nanodisk by $b = 155$ nm; that is, it is located 45 nm away from the disk surface. The inset shows the emission diagram at the indicated spectral position. The directivity of the silicon disk nanoantenna associated with maximum FBR reaches a value of 6. The emission of the dipole is mainly directed into one direction by the silicon disk over the entire spectral range as manifested by values for the FBR larger than unity. The optimum calculated FBR peaks at a vacuum wavelength of 1111 nm, reaching a value of 5521, which is the highest FBR ever reported for single-element nanoantennas.

CONCLUSIONS

We have demonstrated that the electric and magnetic resonances of individual subwavelength silicon nanodisks can be spectrally tuned with respect to each other and brought into spectral overlap by variation of the nanodisk aspect ratio. This ability to individually tune the resonances provides direct control over their interplay. Most importantly, strong directional radiation effects can be obtained by tailoring interference between modes of different character within the same dielectric nanoparticle. We have theoretically investigated this

concept using both an approach based on discrete-dipole approximation and finite-integral frequency-domain calculations. To verify our findings experimentally we have fabricated and optically characterized arrays of silicon nanodisks embedded into a low-index medium, which feature both electric and magnetic resonances in the near-infrared spectral range. Measured transmittance spectra show that the mode overlap renders the silicon disk sample more transparent owing to the destructive interference of resonant backscattering

from two different modes within the same nanodisk, or in other words, indicating improved impedance matching due to a simultaneous electric and magnetic optical response of the silicon nanoparticle arrays. Our experimental results are in excellent agreement with numerical analyses, which further reveal that an ultrahigh front-to-back ratio can be achieved for the emission from a dipole source using a single silicon disk with tailored resonances as a highly directional all-dielectric nanoantenna.

METHODS

For the fabrication of silicon disks embedded into a low-index matrix, we first perform electron-beam lithography on silicon-on-insulator wafers (SOITEC, 220 nm top silicon thickness, 2 μm buried oxide thickness, backside polished) using the negative-tone resist NEB-31A. After cleaning the top silicon surface by oxygen plasma (2 min, 200 W) we spin-coat HDMS as adhesion promoter (3000–4000 rpm, 30 s), directly followed by spin-coating of the electron-beam resist (3000–4000 rpm, 30 s). We perform both a pre-exposure bake (110 °C, 2 min) and a postexposure bake (90 °C, 2 min). For development we insert the sample into MF-321 developer for 40 s followed by rinsing it in deionized water for several minutes. The resulting photoresist pattern is then used as an etch mask for a directive reactive-ion etching process. We stop the etching process precisely when the etch depth reaches the buried oxide layer using *in situ* optical monitoring. The remaining electron-beam resist mask is removed by inserting the etched sample into oxygen plasma.

To embed the silicon disks in a homogeneous optical environment, we overgrow the disks with 550 nm of SiO₂ using low-pressure chemical vapor deposition (LPCVD) and tetra-ethyl-ortho-silicate (TEOS) as precursor (Tystar Tytan 4600, 745 °C, 250 mtorr, 43 min), planarize the surface by reactive-ion etching, and apply three layers of spin-on dielectric (IC1-200 Futurrex, 3000 rpm, 90 s). After spin-coating each single layer the sample is placed on a hot plate (120 °C) for 60 s, and finally we bake it in a convection oven at 120 °C for 30 min. This overall procedure allows us to embed the disks in a flat layer of low-index material while ensuring that no air voids are formed in the proximity of the silicon disks.

Conflict of Interest: The authors declare no competing financial interest.

Acknowledgment. This work was performed, in part, at the Center for Integrated Nanotechnologies, an Office of Science User Facility operated for the U.S. Department of Energy (DOE) Office of Science. Sandia National Laboratories is a multiprogram laboratory managed and operated by Sandia Corporation, a wholly owned subsidiary of Lockheed Martin Corporation, for the U.S. Department of Energy's National Nuclear Security Administration under contract DE-AC04-94AL85000. The authors also acknowledge support from the Australian Research Council. We thank W. Liu, A. Evlyukhin, and A. Kuznetsov for the useful discussions.

REFERENCES AND NOTES

- Novotny, L.; Hecht, B. *Principles of Nano-Optics*; Cambridge University Press: Oxford, UK, 2006.
- Kawata, S.; Ohtsu, M.; Irie, M. *Nano-Optics*; Springer-Verlag: Berlin, 2002.
- Giannini, V.; Fernández-Domínguez, A. I.; Heck, S. C.; Maier, S. A. Plasmonic Nanoantennas: Fundamentals and their Use in Controlling the Radiative Properties of Nanoemitters. *Chem. Rev.* **2011**, *111*, 3888–3912.
- Curto, A. G.; Volpe, G.; Taminiau, T. H.; Kreuzer, M. P.; Quidant, R.; van Hulst, N. F. Unidirectional Emission of a Quantum Dot Coupled to a Nanoantenna. *Science* **2010**, *329*, 930–933.
- Kosako, T.; Kadoya, Y.; Hofmann, H. F. Directional Control of Light by a Nano-optical Yagi-Uda Antenna. *Nat. Photon.* **2010**, *4*, 312–315.
- Miroshnichenko, A. E.; Maksymov, I. S.; Davoyan, A. R.; Simovski, C.; Belov, P.; Kivshar, Yu. S. An Arrayed Nanoantenna for Broadband Light Emission and Detection. *Phys. Status Solidi RRL* **2011**, *5*, 347–349.
- Staude, I.; Maksymov, I. S.; Decker, M.; Miroshnichenko, A. E.; Neshev, D. N.; Jagadish, C.; Kivshar, Yu. S. Broadband Scattering by Tapered Nanoantennas. *Phys. Status Solidi RRL* **2012**, *6*, 466–468.
- Maksymov, I. S.; Staude, I.; Miroshnichenko, A. E.; Kivshar, Yu. S. Optical Yagi-Uda Nanoantennas. *Nanophotonics* **2012**, *1*, 65–81.
- Bohren, C. F.; Huffman, D. R. *Absorption and Scattering of Light by Small Particles*; John Wiley & Sons Inc: New York, 1983.
- Evlyukhin, A. B.; Reinhardt, C.; Seidel, A.; Luk'yanchuk, B. S.; Chichkov, B. N. Optical Response Features of Si-Nanoparticle Arrays. *Phys. Rev. B* **2010**, *82*, 045404.
- Garcia-Exarri, A.; Gómez-Medina, R.; Froufe-Pérez, L. S.; López, C.; Chantada, L.; Scheffold, F.; Aizpurua, J.; Nieto-Vesperinas, M.; Sáenz, J. J. Strong Magnetic Response of Submicron Silicon Particles in the Infrared. *Opt. Express* **2011**, *19*, 4815–4826.
- Evlyukhin, A. B.; Novikov, S. M.; Zywietz, U.; Eriksen, R.-L.; Reinhardt, C.; Bozhevlyni, S. I.; Chichkov, B. N. Demonstration of Magnetic Dipole Resonances of Dielectric Nanospheres in the Visible Region. *Nano Lett.* **2012**, *12*, 3749–3755.
- Kuznetsov, A. I.; Miroshnichenko, A. E.; Fu, Y. H.; Zhang, J.; Luk'yanchuk, B. Magnetic Light. *Sci. Rep.* **2012**, *2*, 492.
- Ginn, J. C.; Brener, I.; Peters, D. W.; Wendt, J. R.; Stevens, J. O.; Hines, P. F.; Basilio, L. I.; Warne, L. K.; Ihlefeld, J. F.; Clem, P. G.; et al. Realizing Optical Magnetism from Dielectric Metamaterials. *Phys. Rev. Lett.* **2012**, *108*, 097402.
- Fu, Y.-H.; Kuznetsov, A. I.; Miroshnichenko, A. E.; Yu, Y. F.; Luk'yanchuk, B. Directional Visible Light Scattering by Silicon Nanoparticles. *Nat. Commun.* **2013**, *4*, 1527–1–1527–6.
- Shi, L.; Harris, J. T.; Fenollosa, R.; Rodriguez, I.; Lu, X.; Korgel, B. A.; Meseguer, F. Monodisperse Silicon Nanocavities and Photonic Crystals with Magnetic Response in the Optical Region. *Nat. Commun.* **2013**, *4*, 1904–1–1904–7.
- Zhao, Q.; Zhou, J.; Zhang, F.; Lippens, D. Mie Resonance-Based Dielectric Metamaterials. *Mater. Today* **2009**, *12*, 60–69.
- Soukoulis, C. M.; Wegener, M. Past Achievements and Future Challenges in the Development of Three-Dimensional Photonic Metamaterials. *Nat. Photon.* **2011**, *5*, 523–530.
- Miroshnichenko, A. E.; Luk'yanchuk, B.; Maier, S. A.; Kivshar, Yu. S. Optically Induced Interaction of Magnetic Moments in Hybrid Metamaterials. *ACS Nano* **2012**, *6*, 837–842.
- Krasnok, A. E.; Miroshnichenko, A. E.; Belov, P. A.; Kivshar, Yu. S. All-Dielectric Optical Nanoantennas. *Opt. Exp.* **2012**, *20*, 20599–20604.

21. Filonov, D. S.; Krasnok, A. E.; Slobozhanyuk, A. P.; Kapitanova, P. V.; Nenasheva, E. A.; Kivshar, Yu. S.; Belov, P. A. Experimental Verification of the Concept of All-Dielectric Nanoantennas. *Appl. Phys. Lett.* **2012**, *100*, 201113–1–201113–4.
22. Devilez, A.; Stout, B.; Bonod, N. Compact Metallo-Dielectric Optical Antenna for Ultra Directional and Enhanced Radiative Emission. *ACS Nano* **2010**, *4*, 3390–3396.
23. Zou, L.; Withayachumnankul, W.; Shah, C. M.; Mitchell, A.; Bhaskaran, M.; Sriram, S.; Fumeaux, C. Dielectric Resonator Nanoantennas at Visible Frequencies. *Opt. Express* **2013**, *21*, 1344–1352.
24. Evlyukhin, A. B.; Kuznetsov, A. I.; Novikov, S. M.; Beermann, J.; Reinhardt, C.; Kiyan, R.; Bozhevolnyi, S. I.; Chichkov, B. N. Optical Properties of Spherical Gold Mesoparticles. *Appl. Phys. B: Laser Opt.* **2012**, *106*, 841–848.
25. Enkrich, C.; Wegener, M.; Linden, S.; Burger, S.; Zschiedrich, L.; Schmidt, F.; Zhou, J. F.; Koschny, Th.; Soukoulis, C. M. Magnetic Metamaterials at Telecommunication and Visible Frequencies. *Phys. Rev. Lett.* **2005**, *95*, 203901.
26. Miroshnichenko, A. M.; Kivshar, Yu. S. Fano Resonances in All-Dielectric Oligomers. *Nano Lett.* **2012**, *12*, 6459–6463.
27. Hao, F.; Sonnefraud, Y.; Van Dorpe, P.; Maier, S. A.; Halas, N. J.; Nordlander, P. Symmetry Breaking in Plasmonic Nanocavities: Subradiant LSPR Sensing and a Tunable Fano Resonance. *Nano Lett.* **2008**, *8*, 3983–3988.
28. Verellen, N.; Sonnefraud, Y.; Sobhani, H.; Hao, F.; Moshchalkov, V. V.; Van Dorpe, P.; Nordlander, P.; Maier, S. A. Fano Resonances in Individual Coherent Plasmonic Nanocavities. *Nano Lett.* **2009**, *9*, 1663–1667.
29. Luk'yanchuk, B.; Zheludev, N. I.; Maier, S. A.; Halas, N. J.; Nordlander, P.; Giessen, H.; Chong, C. T. The Fano Resonance in Plasmonic Nanostructures and Metamaterials. *Nat. Mater.* **2010**, *9*, 707–715.
30. Chen, H.; Shao, L.; Ming, T.; Woo, K. C.; Man, Y. C.; Wang, J.; Lin, H.-Q. Observation of the Fano Resonance in Gold Nanorods Supported on High-Dielectric-Constant Substrates. *ACS Nano* **2011**, *5*, 6754–6763.
31. Garcia-Camara, B.; Moreno, F.; Gonzalez, F.; Martin, O. J. F. Light Scattering by an Array of Electric and Magnetic Nanoparticles. *Opt. Express* **2010**, *18*, 10001–10015.
32. Nieto-Vesperinas, M.; Gomez-Medina, R.; Saenz, J. J. Angle-Suppressed Scattering and Optical Forces on Submicrometer Dielectric Particles. *J. Opt. Soc. Am. A* **2011**, *28*, 54–60.
33. García-Cámarra, B.; Alcaraz de la Osa, R.; Saiz, J. M.; González, F.; Moreno, F. Directionality in Scattering by Nanoparticles: Kerker's Null-Scattering Conditions Revisited. *Opt. Lett.* **2011**, *36*, 728–730.
34. Gómez-Medina, R.; García-Cámarra, B.; Suárez-Lacalle, I.; González, F.; Moreno, F.; Nieto-Vesperinas, M.; Sáenz, J. J. Electric and Magnetic Dipolar Response of Germanium Nanospheres: Interference Effects, Scattering Anisotropy, and Optical Forces. *J. Nanophoton.* **2011**, *5*, 053512–1–053512–9.
35. Person, S.; Jain, M.; Lapin, Z.; Sáenz, J. J.; Wicks, G.; Novotny, L. Demonstration of Zero Optical Backscattering from Single Nanoparticles. *Nano Lett.* **2013**, *13*, 1806–1809.
36. Geffrin, J. M.; García-Cámarra, B.; Gómez-Medina, R.; Alberla, P.; Froufe-Pérez, L. S.; Eyraud, C.; Litman, A.; Vaillon, R.; González, F.; Nieto-Vesperinas, M.; et al. Magnetic and Electric Coherence in Forward- and Back-Scattered Electromagnetic Waves by a Single Dielectric Subwavelength Sphere. *Nat. Commun.* **2012**, *3*, 1171–1–1171–8.
37. Kerker, M.; Wang, D. S.; Giles, C. L. Electromagnetic Scattering by Magnetic Spheres. *J. Opt. Soc. Am.* **1983**, *73*, 765–767.
38. Liu, W.; Miroshnichenko, A. E.; Neshev, D. N.; Kivshar, Yu. S. Broadband Unidirectional Scattering by Magneto-Electric Core–Shell Nanoparticles. *ACS Nano* **2012**, *6*, 5489–5497.
39. Pakizeh, T.; Kall, M. Unidirectional Ultracompact Optical Nanoantennas. *Nano Lett.* **2009**, *9*, 2343–2349.
40. Spinelli, P.; Verschuur, M. A.; Polman, A. Omnidirectional Antireflection Coating Based on Subwavelength Surface Mie Resonators. *Nat. Commun.* **2012**, *3*, 692–1–692–5.
41. Evlyukhin, A. B.; Reinhardt, C.; Chichkov, B. N. Multipole Light Scattering by Nonspherical Nanoparticles in the Discrete Dipole Approximation. *Phys. Rev. B* **2011**, *84*, 235429–1–235429–8.
42. Rolly, B.; Stout, B.; Bonod, N. Boosting the Directivity of Optical Antennas with Magnetic and Electric Dipolar Resonant Particles. *Opt. Express* **2012**, *20*, 20376–20386.
43. Draine, B. T.; Flatau, P. J. Discrete-Dipole Approximation for Scattering Calculations. *J. Opt. Soc. Am.* **1994**, *A11*, 1491–1499.
44. Long, S. A.; McAllister, M.; Shen, L. C. The Resonant Cylindrical Dielectric Cavity Antenna. *IEEE Trans. Antennas Propag.* **1983**, *31*, 406–412.
45. Husnik, M.; Linden, S.; Diehl, R.; Niegemann, J.; Busch, K.; Wegener, M. Quantitative Experimental Determination of Scattering and Absorption Cross-Section Spectra of Individual Optical Metallic Nanoantennas. *Phys. Rev. Lett.* **2012**, *109*, 233902.
46. Miroshnichenko, A. E. Off-Resonance Field Enhancement by Spherical Nanoshells. *Phys. Rev. A* **2010**, *81*, 053818.